Numerical homogenization of cracking processes in thin fibre-epoxy layers

M.V. Cid Alfaro, A.S.J. Suiker, C.V. Verhoosel, R. de Borst

Title: Numerical homogenization of cracking processes in thin fibre-epoxy layers

Authors: M.V. Cid Alfaro, A.S.J. Suiker, C.V. Verhoosel, R. de Borst

PII: S0997-7538(09)00117-X

DOI: 10.1016/j.euromechsol.2009.09.006

Reference: EJMSOL 2552

To appear in: *European Journal of Mechanics / A Solids*

Received Date: 18 May 2009

Revised Date: 28September2009

Accepted Date: 30 September 2009

Please cite this article as: Alfaro, M.V.C., Suiker, A.S.J., Verhoosel, C.V., de Borst, R. Numerical homogenization of cracking processes in thin fibre-epoxy layers, European Journal of Mechanics / A Solids (2009), doi: 10.1016/j.euromechsol.2009.09.006

Numerical homogenization of cracking processes in thin fibre-epoxy layers

M.V. Cid Alfaro[1], A.S.J. Suiker[1], C.V. Verhoosel[1] and R. de Borst[2].

1: Delft University of Technology, P.O. Box 5058, NL-2600 GB, Delft, The Netherlands
2: Eindhoven University of Technology, P.O. Box 513, NL-5600 MB, Eindhoven, The Netherlands

Abstract

Discrete microscale fracture processes in thin fibre-epoxy layers are connected to a mesoscale traction-separation law through a numerical homogenization framework. The microscale fracture processes are studied with the finite element method, where cracking within the epoxy and debonding between fibres and epoxy is simulated by placing interface elements furnished with a mixed-mode interface damage model in between the continuum elements modelling the fibres and epoxy. It is demonstrated how the effective traction-separation response and the corresponding microscale fracture patterns under mesoscale tensile conditions depend on the sample size, the fibre volume fraction and the presence of imperfections.

Key words: fibre debonding, matrix cracking, cohesive zone model, discrete fracture, adhesive layers.

1. Introduction

Finite element simulations serve as an important tool for studying the complex failure behaviour of fibre-epoxy systems and optimizing their performance in (macroscopic) engineering applications. However, the execution of a direct numerical simulation on the mechanical response of an engineering structure, where all the details of the underlying microstructure are incorporated, requires a very fine finite element mesh, thus leading to an impractical amount of computational time. A more efficient approach for this purpose is to use material models that represent the mechanical response of the underlying microstructure in an effective fashion, as derived by means of analytical and/or numerical homogenization techniques.

Analytical homogenization techniques often lead to computationally efficient models. Nevertheless, these models typically fail to describe the effective material response accurately when the underlying microstructure is complex and is characterised by a strongly non-linear constitutive behaviour. Under these conditions the use of a numerical homogenization method is recommendable. In the case of continuum models, numerical homogenization is based on computationally averaging the generated microstructural stress and deformation over a representative volume element (RVE), thereby implicitly (i.e., not in closed-form) establishing an effective, mesoscopic constitutive relation between the average stress and deformation. Over the past two decades, various approaches have been developed along this line, see for example [1, 2, 3, 4, 5, 6, 7, 8, 9]. These approaches rely on a local periodicity of the microstructure in the direct neighborhood of the RVE, but do not impose periodicity over the complete macroscopic structure under consideration (i.e., global periodicity is not required). The macroscopic structure thus contains mesoscopic material points for which the specific microscopic RVE's are assumed to be periodic only in a small vicinity of the material points.

Although numerical homogenization approaches for bulk continuum problems have been reported widely in the literature, numerical homogenization frameworks for thin layer problems are lacking. Only recently a first step into this direction has been made by Geubelle and co-workers [10, 11], where a mesoscale cohesive zone formulation was derived from numerically homogenizing the microscale failure processes in a thin, heterogeneous adhesive, as simulated with an isotropic damage model. The present paper also focuses on the derivation of a mesoscale cohesive zone model from the numerical homogenization of microscale fracture processes in a thin layer. The homogenization framework developed here shows similarities with that of Geubelle and co-workers [10, 11]. It is essentially obtained as a special case of the numerical homogenization of a bulk material sample loaded under periodic boundary conditions, by collapsing the mesoscale thickness of the bulk sample into a (cohesive) surface, but the derivation of the homogenization framework runs along different lines. In addition, instead of simulating the microscale fracture processes in an averaged, smeared fashion using a continuum damage model, a cohesive zone model is applied. This is, since experimental observations show that the microscale failure behaviour of relatively brittle fibre-epoxy systems is characterised by fibre decohesion and matrix cracking along well-identifiable, discrete cracking paths [12, 13, 14].

In order to allow for arbitrary microscale cracking paths that may develop from complex crack branching and crack coalescence mechanisms, in the applied finite element discretizations interface elements are placed between all contin-

uum elements simulating the epoxy material. Furthermore, interface elements are placed between the fibres and the epoxy matrix. This modelling approach, which was originally proposed by Xu and Needleman [15], has been successfully used in failure analyses of various materials, such as crazing in polymers [16], and quasi-brittle fracture in cementitious materials [17].

The mesoscale traction-separation curve is constructed from numerically homogenizing the fracture response of a periodic fibre-epoxy microstructure loaded under uniaxial tension. Such a traction-separation curve can, for example, be applied in material points of interface elements used for simulating mesoscopic fracture in fibre adhesives, under the condition that the thickness of the adhesive is negligible with respect to the length scales of the macroscopic structure considered (i.e., a separation of length scales can be warranted). Nonetheless, the analysis of specific meso- and/or macroscale applications falls beyond the scope of the present study; the attention is directed here to the numerical homogenization of the response of a microstructural RVE to a mesoscopic traction-separation curve, thereby considering the influence of the fibre volume fraction and local imperfections. Although the numerical examples treated focus upon uniaxial tension, the homogenization framework presented is applicable to arbitrary, mixed-mode loading conditions.

The organization of this paper is as follows. In Section 2 the interface damage model used for simulating the microscale fracture is summarised. In Section 3 the governing equations of the fibre-epoxy material are formulated at the meso- and microscales. The numerical homogenization framework that connects the fracture behaviour of the microstructural fibre-epoxy sample to a mesoscopic traction-separation response is presented in Section 4. In Section 5 the applicability of the numerical homogenization framework is demonstrated by studying fibre-epoxy samples loaded under uniaxial tension. The convergence of the RVE size is examined, as well as the effect of the fibre volume fraction and the presence of imperfections on the traction-separation response. Finally, in Section 6 the main conclusions of the study are summarised.

2. Review of the interface damage model

In the present study the modelling of matrix cracking and fibre-matrix debonding is performed with interface elements endowed with a rate-dependent damage model. The damage model used has been explained in detail in [18, 19], in which it has been applied to study the mesoscale laminate failure mechanisms reported in [20, 21]. The damage model is phenomenological, and has a bi-linear traction-

separation curve to model a quasi-brittle failure response generated by two separating crack faces, see Figure 1. For completeness, only the main equations of the interface damage model in [18, 19] are summarised below. In the presentation of the model equations, adaptations are made to apply the three-dimensional model in [19] to the two-dimensional configurations studied in this paper. The constitutive equation relating the tractions to the relative displacements across an interface is given by

$$t_i = (1-d)K\delta_{ij}v_j - dC_{ij}\delta_{1j}\langle -v_1\rangle \qquad \text{where} \qquad i,j \in \{1,2\}, \tag{1}$$

with the normal and shear components of the tractions t_i and relative displacements v_i designated by the indices '1' and '2', respectively. Furthermore, K is the elastic stiffness and δ_{ij} is the Kronecker delta symbol. The damage parameter d is bounded as $0 \leq d \leq 1$, such that an undamaged integration point is represented by $d = 0$ and a completely damaged integration point is reflected by $d = 1$. Penetration of two opposite crack faces is prevented by the second term in the right-hand side of Eq.(1), where the Macauley brackets $\langle x\rangle = \frac{1}{2}(x + |x|)$ ensure that crack faces interact elastically when the normal relative displacement v_1 becomes negative. The evolution of damage is assumed to occur in a rate-dependent fashion,

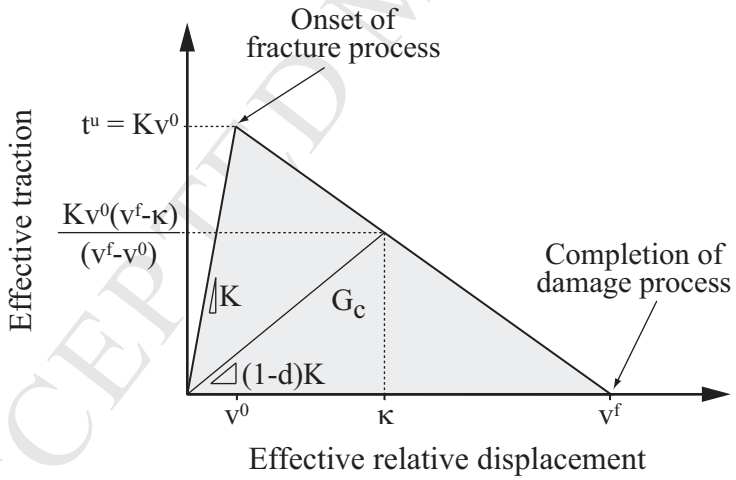

Figure 1: Traction-separation law.

with the rate of damage formulated as

$$\dot{d} = \begin{cases} \dfrac{\hat{F}(\lambda,\kappa)}{\eta} & \text{for} \quad \lambda \geq \kappa \quad \text{and} \quad v^0 \leq \kappa < v^f \,, \\ 0 & \text{for} \quad 0 \leq \lambda < \kappa \quad \text{or} \quad \kappa = v^f \,. \end{cases} \tag{2}$$

Here, η is a relaxation parameter (with dimension of time) and $\hat{F}(\lambda,\kappa)$ is the damage loading function, which is dependent upon a deformation measure λ and a history variable κ. The deformation measure λ is taken as the Euclidean norm of the vector of relative crack face displacements, $\lambda = \|\boldsymbol{v}\| = \sqrt{v_1^2 + v_2^2}$. The upper expression in Eq.(2) defines the rate of damage when the effective deformation λ exceeds the value of the history variable κ, whereas the lower expression sets the rate of damage equal to zero when (i) the threshold value for the initiation of damage has not (yet) been reached, (ii) the interfacial material point is in a state of unloading, or (iii) the damage process has been completed. Note from Eq.(2) that the history parameter is bounded as $v^0 \leq \kappa \leq v^f$, with v^0 and v^f the relative crack face displacements at damage initiation ($d = 0$) and damage completion ($d = 1$), respectively.

The actual form of the damage loading function $\hat{F}(\lambda,\kappa)$ is connected to the shape of the softening curve in the traction-separation relation, see [19] for more details. As illustrated in Figure 1, the damage process is characterised by a linear softening curve, which is in correspondence with the following damage loading function:

$$\hat{F}(\lambda,\kappa) \;=\; \hat{f}(\lambda) - \hat{d}(\kappa) \;=\; \frac{v^f(\lambda - v^0)}{\lambda(v^f - v^0)} \;-\; \frac{v^f(\kappa - v^0)}{\kappa(v^f - v^0)} \,. \tag{3}$$

It can be observed from Eq.(2) that in the limit case of the relaxation parameter going to zero, $\eta \to 0$, the rate-independent loading condition is recovered: $\hat{F}(\lambda,\kappa) = 0$, which, as shown by Eq.(3), corresponds to $\lambda = \kappa$.

In order to simulate fracture processes of arbitrary mode-mixity, the relative displacements at damage initiation, v^0, and damage completion, v^f, are made dependent of a mode-mixity parameter β, see also [22], i.e.,

$$\beta = \frac{v_2}{v_2 + \langle v_1 \rangle} \,. \tag{4}$$

In correspondence with this expression, under pure mode I loading conditions $v_2 = 0$ and thus $\beta = 0$, whereas under pure mode II loading conditions $v_1 = 0$

and thus $\beta = 1$. The functions $v^0 = \hat{v}^0(\beta)$ and $v^f = \hat{v}^f(\beta)$ can be computed adopting an energy-based, mixed-mode failure criterion from linear elastic fracture mechanics, see [19, 22]. For this purpose, a fracture criterion is taken that is often used to characterize mixed-mode toughness data for brittle interfacial fracture [23, 24]:

$$\frac{G_I}{G_{I,c}} + \frac{G_{II}}{G_{II,c}} = 1\,, \tag{5}$$

with G_I and G_{II} the mode I and mode II energy release rates, and $G_{I,c}$ and $G_{II,c}$ the toughnesses under pure mode I and pure mode II loading conditions respectively. From Eqs. (4) and (5), the effective relative displacements at damage initiation and damage completion can be, respectively, computed as

$$v^0 = \hat{v}^0(\beta) = v_1^0\, v_2^0 \sqrt{\frac{1 + 2\beta^2 - 2\beta}{\left(\beta v_1^0\right)^2 + \left((1-\beta) v_2^0\right)^2}}\,, \tag{6}$$

and

$$v^f = \hat{v}^f(\beta) = \frac{2(1 + 2\beta^2 - 2\beta)}{K v^0} \left[\left(\frac{(1-\beta)^2}{G_{I,c}} \right) + \left(\frac{\beta^2}{G_{II,c}} \right) \right]^{-1}\,, \tag{7}$$

where $v_1^0 = t_1^u / K$ and $v_2^0 = t_2^u / K$ are the relative displacements at which damage initiates under pure mode I and pure mode II loading conditions, respectively, and t_1^u and t_2^u are the ultimate tractions under pure mode I and pure mode II conditions, respectively. More details about the above interface damage model and its numerical discretization can be found in [19].

3. Micro- and mesoscale modelling

Consider a mesoscopic domain $\Omega^M \subset \mathbb{R}^2$ with an external boundary Γ^M, see Figure 2. The external boundary is subjected to displacements $\boldsymbol{u}^M$ and tractions $\boldsymbol{t}^M$ at Γ_u^M and Γ_t^M, respectively. The mesoscopic domain is crossed by an adhesive layer Γ_{coh}^M. The response in a material point of the adhesive layer is connected to the lower-scale response of a heterogeneous, microscopic domain $\Omega^m \subset \mathbb{R}^2$. The microscopic domain is represented by a fibre-epoxy sample of width b. Fracture in the microscopic domain occurs along the cracking path Γ_{coh}^m. The boundary conditions at the outer edges Γ^m of the microscopic domain are assumed to be periodic. Further, for establishing a connection between formulations at the meso- and microscale levels, it is assumed that the microscopic domain can be considered as a representative volume element (RVE).

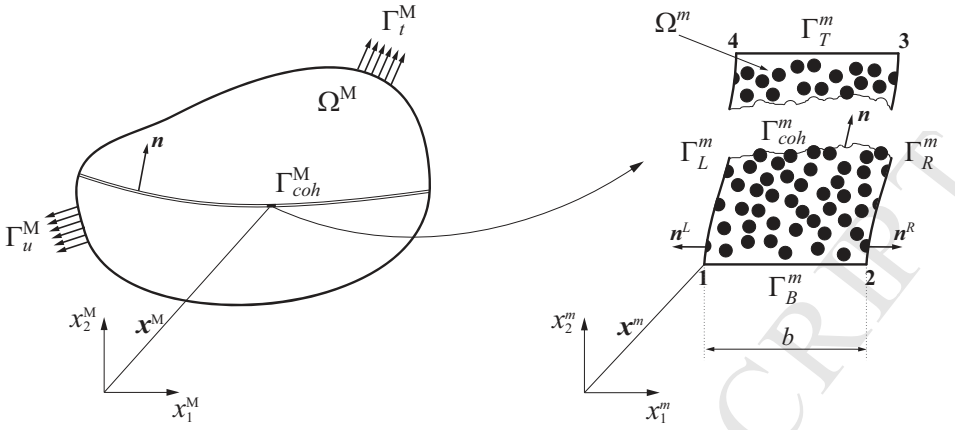

Figure 2: Mesoscopic domain Ω^M (left) and microscopic domain Ω^m (right). The mesoscopic domain is crossed by an adhesive layer Γ_{coh}^M. The failure behaviour in a material point of the adhesive layer is connected to the failure response of the microscopic domain (i.e., a fibre-epoxy sample), as characterised by cracking across the domain width b along the internal boundary Γ_{coh}^m. The boundary conditions at the outer edges Γ^m of the microscopic domain are periodic.

3.1. Governing equations at the mesoscale

The equilibrium condition for an arbitrary material point in the mesoscopic domain Ω^M depicted in Figure 2 is

$$\sigma_{ij,j}^M = 0 \qquad \text{in } \Omega^M, \tag{8}$$

where σ_{ij}^M represents the Cauchy stress, with the superscript M denoting the mesoscopic character of the variable. The tensor indices can have the values $i, j \in \{1, 2\}$, in correspondence with the two-dimensional, orthogonal coordinate system shown in Figure 2. Note that, for reasons of convenience, the body forces have been omitted in Eq.(8). In addition, the boundary conditions for the mesoscopic domain are given by

$$\sigma_{ij}^M n_j = t_i^M \qquad \text{on } \Gamma_t^M, \tag{9}$$

$$u_i^M = \hat{u}_i^M \qquad \text{on } \Gamma_u^M, \tag{10}$$

where t_i^M and $\hat{u}_i^M$ respectively are the tractions and displacements, as prescribed on the corresponding external boundaries Γ_t^M and Γ_u^M with outward normal n_i. Note that the total external boundary is given by $\Gamma^M = \Gamma_t^M \cup \Gamma_u^M$. The cohesive

surface Γ^M_{coh} can be considered as an internal boundary, for which the tractions t^M_i are related to the Cauchy stress σ^M_{ij} through the equilibrium condition

$$\sigma^M_{ij} n_j = t^M_i \qquad \text{on } \Gamma^M_{coh}. \tag{11}$$

Applying the standard variational method, the principle of virtual work at the mesoscale, under the neglection of body forces, leads to the following expression

$$\int_{\Omega^M} \sigma^M_{ij}\, \delta\varepsilon^M_{ij}\, d\Omega^M + \underbrace{\int_{\Gamma^M_{coh}} t^M_i\, \delta[\![u^M_i]\!]\, d\Gamma^M_{coh}}_{\delta W^M_{coh}} = \int_{\Gamma^M_t} t^M_i\, \delta u^M_i\, d\Gamma^M_t, \tag{12}$$

which holds for any admissible variational mesoscale displacement δu^M_i. Here, ε^M_{ij} represents the mesoscopic engineering strain, and the symbol $[\![\bullet]\!] = (\bullet^+ - \bullet^-)$ denotes the jump of a quantity (i.e., the displacement) across the cohesive surface, with $\pm$ designating the upper and lower faces of the cohesive surface. As can be observed from the above expression, the quantity δW^M_{coh} represents the virtual work of the cohesive surface.

3.2. Governing equations at the microscale

Similar to the mesoscale equilibrium condition (8), the equilibrium requirement for a material point within the microscopic RVE Ω^m shown in Figure 2 can be expressed as

$$\sigma^m_{ij,j} = 0 \qquad \text{in } \Omega^m, \tag{13}$$

where the boundary conditions are

$$\sigma^m_{ij} n_j = t_i \qquad \text{on } \Gamma^m_t, \tag{14}$$

$$u_i = \hat{u}_i \qquad \text{on } \Gamma^m_u. \tag{15}$$

Here, t_i and $\hat{u}_i$ are the tractions and displacements at the corresponding external boundaries Γ^m_t and Γ^m_u of the microscopic RVE, with the superscript m indicating the microscopic character of these parameters. The total external boundary of the RVE is given by $\Gamma^m = \Gamma^m_t \cup \Gamma^m_u$. In order to keep the notation in forthcoming sections concise, the index m will *not* be used for all microscale variables introduced

in this section, i.e., note that it has been omitted for the tractions t_i and the displacements u_i in Eqs.(14) and (15). As a next step, equilibrium at the microscale cohesive surface Γ^m_{coh} is prescribed by

$$\sigma^m_{ij} n_j = t_i \qquad \text{on } \Gamma^m_{coh}. \tag{16}$$

Similar to Eq.(12), the principle of virtual work at the microscale leads to

$$\int_{\Omega^m} \sigma^m_{ij}\, \delta\varepsilon^m_{ij}\, d\Omega^m + \int_{\Gamma^m_{coh}} t_i\, \delta[\![u_i]\!]\, d\Gamma^m_{coh} = \int_{\Gamma^m_t} t_i\, \delta u_i\, d\Gamma^m_t\,, \tag{17}$$

which must be satisfied for any admissible variational microscale displacement δu_i. In the above expression, ε^m_{ij} is the microscale strain tensor.

4. Connection between the microscale and mesoscale

In order to establish a connection between the responses of the microscale and mesoscale domains shown in Figure 2, the microscale displacement field u_i is expressed in terms of the mesoscale displacement field u^M_i and a fluctuating displacement field $\tilde{u}_i$ as

$$u_i(x^M_j, x^m_k) = u^M_i(x^M_j) + \tilde{u}_i(x^m_k)\,, \tag{18}$$

where, as illustrated in Figure 2, x^M_j and x^m_k denote the locations of the mesoscale and microscale material points at which u^M_i and $\tilde{u}_i$ are evaluated, respectively. Essentially, the fluctuating displacement field $\tilde{u}_i$ accounts for the displacement variations generated by the microstructural inhomogeneities, as measured with respect to the (average) mesoscopic displacement of the microscale RVE.

4.1. Formulation of boundary conditions on the RVE

In correspondence with the decomposition given by Eq.(18), periodic boundary conditions for the microscale RVE can be formulated as

$$\begin{aligned}
&\tilde{u}^T_i(s_1) = \tilde{u}^B_i(s_1),\\
&t^T_i(s_1) = -t^B_i(s_1),\\
&\tilde{u}^L_i(s_2) = \tilde{u}^R_i(s_2),\\
&t^L_i(s_2) = -t^R_i(s_2),
\end{aligned} \tag{19}$$

where s_1 is a local coordinate along the Γ_T^m and Γ_B^m boundaries of the RVE, and s_2 is a local coordinate along the Γ_L^m and Γ_R^m boundaries of the RVE. The first two boundary conditions for the Top (T) and bottom (B) edges of the RVE reflect the periodicity in the x_2^m-direction, where the second boundary condition ensures that the total work generated by the periodic boundary conditions is zero. Similarly, the last two boundary conditions for the left (L) and right (R) edges of the RVE warrant periodicity in the x_1^m-direction.

The displacements of the four corner nodes of the microscale RVE in Figure 2 correspond to the (uniform) mesoscopic deformation of a material point in the cohesive interface Γ_{coh}^M. Hence, the displacement jump across the mesoscale cohesive interface may be expressed in terms of the displacement difference of two opposite corner nodes at the top and bottom surfaces of the RVE as

$$[\![u_i^M]\!] = u_i^{M,T} - u_i^{M,B} = u_i^4 - u_i^1 = u_i^3 - u_i^2. \tag{20}$$

In accordance with this condition, the microscale displacement fluctuations are equal to zero at the four RVE corner nodes, i.e.,

$$\tilde{u}_i^n = 0 \qquad \text{with} \qquad n \in \{1, 2, 3, 4\}. \tag{21}$$

Combining Eqs.(21) and (18) with Eq.(19), the periodic displacement boundary conditions, Eq.(19), may be reformulated as

$$\begin{aligned} u_i^T(s_1) &= u_i^B(s_1) + u_i^4 - u_i^1 \qquad (\text{or, } u_i^T(s_1) = u_i^B(s_1) + u_i^3 - u_i^2), \\ u_i^R(s_2) &= u_i^L(s_2) + u_i^2 - u_i^1 \qquad (\text{or, } u_i^R(s_2) = u_i^L(s_2) + u_i^3 - u_i^4). \end{aligned} \tag{22}$$

The above form of the periodic displacement boundary conditions is suitable for implementation within a finite element code.

4.2. Derivation of the mesoscopic interfacial traction

For establishing an expression for the mesoscopic traction, t_i^M, in a material point at the mesoscale cohesive interface Γ_{coh}^M, the averaging principle proposed by Hill [25] is applied. This principle states that the spatial average of the virtual work at the microscale, $\overline{\delta W^m}$, needs to be equal to the virtual work in a local material point of the mesoscale cohesive interface, δw_{coh}^M, i.e.,

$$\overline{\delta W^m} = \delta w_{coh}^M. \tag{23}$$

Since the local virtual work and total virtual work for the mesoscale cohesive interface are related as

$$\delta W_{coh}^{M} = \int\limits_{\Gamma_{coh}^{M}} \delta w_{coh}^{M} \, d\Gamma_{coh}^{M}, \tag{24}$$

where the total virtual work is given by the second term in Eq.(12), the local virtual work of the mesoscale cohesive interface is expressed by

$$\delta w_{coh}^{M} = t_i^{M} \delta [\![u_i^{M}]\!]. \tag{25}$$

In addition, the average virtual work at the microscale is determined by contributions of the cohesive interface Γ_{coh}^{m} and the adjacent continuum Ω^{m} as

$$\overline{\delta W^{m}} = \frac{1}{b} \delta W^{m} = \frac{1}{b} \left\{ \int\limits_{\Omega^{m}} \sigma_{ij}^{m} \, \delta \varepsilon_{ij}^{m} \, d\Omega^{m} + \int\limits_{\Gamma_{coh}^{m}} t_i \, \delta [\![u_i]\!] \, d\Gamma_{coh}^{m} \right\}. \tag{26}$$

Note from the above expression that the averaging procedure is performed by dividing the total virtual work of the microscale RVE by its width b. The height of the RVE does not need to be taken into account here, since the actual mesoscale geometrical object is a cohesive surface Γ_{coh}^{M} with zero thickness. Invoking Eq.(17), the term in between the curly braces in Eq.(26) may be rewritten as

$$\overline{\delta W^{m}} = \frac{1}{b} \int\limits_{\Gamma_{t}^{m}} t_i \, \delta u_i \, d\Gamma_{t}^{m}. \tag{27}$$

Substituting the displacement decomposition, Eq.(18), into Eq.(27) then leads to

$$\overline{\delta W^{m}} = \frac{1}{b} \left(\int\limits_{\Gamma_{t}^{m}} t_i \, \delta u_i^{M} \, d\Gamma_{t}^{m} + \int\limits_{\Gamma_{t}^{m}} t_i \, \delta \tilde{u}_i \, d\Gamma_{t}^{m} \right). \tag{28}$$

The second integral term in the right-hand side of Eq.(28) may be developed as

$$\begin{aligned}\int_{\Gamma_t^m} t_i\,\delta\tilde{u}_i\,d\Gamma_t^m &= \int_{\Gamma_L^m} t_i^L\delta\tilde{u}_i^L d\Gamma_L^m + \int_{\Gamma_R^m} t_i^R\delta\tilde{u}_i^R d\Gamma_R^m \\ &+ \int_{\Gamma_T^m} t_i^T\delta\tilde{u}_i^T d\Gamma_T^m + \int_{\Gamma_B^m} t_i^B\delta\tilde{u}_i^B d\Gamma_B^m \\ &= \int_{\Gamma_t^m} t_i^T\left(\delta\tilde{u}_i^T - \delta\tilde{u}_i^B\right) ds_1 + \int_{\Gamma_t^m} t_i^R\left(\delta\tilde{u}_i^R - \delta\tilde{u}_i^L\right) ds_2 \\ &= 0,\end{aligned} \tag{29}$$

in which the boundary conditions, Eq.(19) are substituted to arrive at the final result that the microscopic fluctuations field does not contribute to the average microscale virtual work. As mentioned previously, s_1 here is a local coordinate along the Γ_T^m and Γ_B^m boundaries of the RVE, and s_2 is a local coordinate along the Γ_L^m and Γ_R^m boundaries of the RVE. As a next step, the first integral term in the right-hand side of Eq.(28) is developed as

$$\begin{aligned}\int_{\Gamma_t^m} t_i\,\delta u_i^M\,d\Gamma_t^m &= \int_{\Gamma_L^m} t_i^L\delta u_i^{M,L} d\Gamma_L^m + \int_{\Gamma_R^m} t_i^R\delta u_i^{M,R} d\Gamma_R^m \\ &+ \int_{\Gamma_T^m} t_i^T\delta u_i^{M,T} d\Gamma_T^m + \int_{\Gamma_B^m} t_i^B\delta u_i^{M,B} d\Gamma_B^m \\ &= \int_{\Gamma_t^m} t_i^T\left(\delta u_i^{M,T} - \delta u_i^{M,B}\right) ds_1 + \int_{\Gamma_t^m} t_i^R\left(\delta u_i^{M,R} - \delta u_i^{M,L}\right) ds_2 \\ &= \left(\delta u_i^4 - \delta u_i^1\right)\int_{\Gamma_t^m} t_i^T ds_1 + \left(\delta u_i^2 - \delta u_i^1\right)\int_{\Gamma_t^m} t_i^R ds_2,\end{aligned} \tag{30}$$

where the periodicity conditions given by Eqs.(19) and (22) are inserted to arrive at the final expression. In order to develop this expression further, the specific boundary conditions of the microscale RVE need to be invoked. Within a finite element setting, the boundary conditions, Eq.(20), can be applied in two different ways, which are depicted in Figure 3 as 'Case 1' and 'Case 2'. The essential difference between these two cases relates to the horizontal displacement of the right corner node at the bottom RVE edge (i.e., node 2), which is unconstrained

for Case 1 and fully constrained for Case 2. Correspondingly, the boundary conditions for Case 1 introduce the following constraints on the RVE

$$\delta u_1^1 = \delta u_2^1 = 0, \qquad \int_{\Gamma_R^m} t_1^R d\Gamma_R^m = 0, \qquad \delta u_2^2 = 0, \tag{31}$$

where the third constraint essentially corresponds to a zero average normal stress in the x_1^m-direction of the RVE (which is in agreement with an unconstrained displacement of node 2 in the x_1^m-direction). In contrast, the boundary conditions for Case 2 imply

$$\delta u_1^1 = \delta u_2^1 = 0, \qquad \delta u_1^2 = \delta u_2^2 = 0, \tag{32}$$

where the third constraint in the above expression corresponds to a zero displacement of node 2 in the x_1^m-direction of the RVE. Despite the different boundary conditions for Cases 1 and 2, substitution of either Eq.(31) or Eq.(32) into Eq.(30) leads to an identical result, namely

$$\int_{\Gamma_t^m} t_i \, \delta u_i^M \, d\Gamma_t^m = \delta u_i^4 \int_{\Gamma_T^m} t_i^T d\Gamma_T^m. \tag{33}$$

Subsequently, inserting Eq.(33) together with Eq.(29) into Eq.(28) gives

$$\overline{\delta W^m} = \frac{1}{b} \int_{\Gamma_T^m} t_i^T d\Gamma_T^m \, \delta u_i^4. \tag{34}$$

In accordance with Eq.(23), this expression needs to be equated with the virtual work in a local material point of the mesoscopic cohesive interface, δw_{coh}^M, given by Eq.(25), which leads to

$$t_i^M \delta [\![u_i^M]\!] = \frac{1}{b} \int_{\Gamma_T^m} t_i^T \, d\Gamma_T^m \, \delta u_i^4 \, . \tag{35}$$

Since $[\![u_i^M]\!] = u_i^4$ for both Case 1 and Case 2, see Figure 3, the above expression generally results in

$$t_i^M = \frac{1}{b} \int_{\Gamma_T^m} t_i^T d\Gamma_T^m. \tag{36}$$

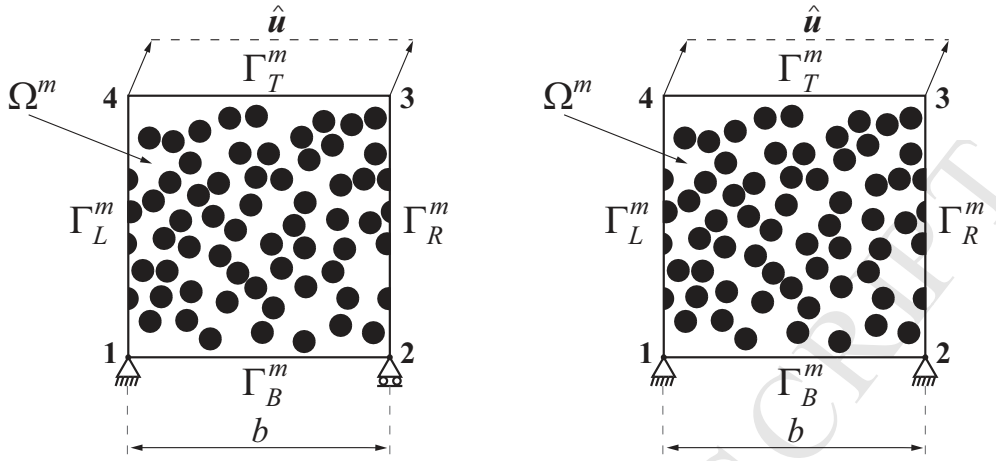

(a) Case 1 (b) Case 2

Figure 3: Two different boundary conditions for the microscale RVE, as indicated at node nr. 2.

Obviously, within a finite element discretization the integral term in the right-hand side of Eq.(36) is approximated by the summation of the nodal forces at the top edge of the RVE. Although Eq.(36) is applicable to both types of RVE boundary conditions depicted in Figure 3, the results computed with this expression will be nevertheless different, as a result of the different responses of the two microscale RVE's. Here, it is difficult to say which of the two RVE's generally provides a more accurate representation for the behaviour at the mesoscale, since this typically depends on the characteristics of the macroscopic boundary value problem problem under consideration. Hence, for the numerical simulations presented in the forthcoming sections, the boundary conditions of the RVE are chosen somewhat arbitrarily in accordance with Case 1.

5. Numerical simulations of a fibre-epoxy specimen subjected to uniaxial tension

In the present section a mesoscale traction-separation curve is derived from the failure response of a microscale fibre-epoxy sample using the homogenization framework presented in Section 4.2. Although the homogenization framework can be applied to samples subjected to arbitrary combinations of tensile and shear loading, for simplicity the examples studied focus upon uniaxial tension.

5.1. Geometry and boundary conditions of the fibre-epoxy samples

An important requirement in a numerical homogenization study is to check whether a loaded specimen converges to an RVE upon an increase in size. In the present communication this convergence study is done for a layer with a specific thickness, thus keeping the length scale in the thickness direction (i.e., the sample height) fixed. In the longitudinal direction the length scale is varied by considering two different sample widths. Note that this approach is different from a convergence study on RVE's for bulk materials, where the length scales in all dimensional directions of the sample are varied, see for example, [9].

For each of the two samples two different fibre volume fractions are considered, i.e., V_f = 0.3 and 0.5, see Figures 4 and 5. The samples are subjected to uniaxial tension by prescribing the vertical displacement, $\hat{u}_2$, at the top edge of the sample. Quasi-static loading conditions are warranted by using a relatively small nominal strain rate of $\dot{\hat{u}}_2/h = 4 \times 10^{-3}\, s^{-1}$, where h is the sample height. Periodic boundary conditions are prescribed at the left and right edges of the sample, as explained in Section 4.1. The displacement at the bottom edge of the sample is constrained in the vertical direction, and the displacement of the node at the bottom-left corner of the specimen is also constrained in the horizontal direction, see Figures 4 and 5. These boundary conditions are in correspondence with Case 1 depicted in Figure 3(a).

The first sample studied is square-shaped, with a width (and height) equal to $b = h = 0.125$ mm. The second sample is rectangular-shaped, where, in comparison with the square-shaped sample, the width is chosen two times larger, i.e., $b = 0.250$ mm, while the height h is kept the same. Essentially, the chosen sample height is representative of the thickness of fibre-epoxy layers used in GLARE [13]. These fibre-epoxy layers are composed of an FM94 epoxy and S2 glass fibres of $10\,\mu$m in diameter. As illustrated in Figures 4 and 5, the internal material structure of the samples relates to a random fibre distribution that is geometrically periodic in the x_1-direction.

5.2. Finite element model

The finite element model used for the microscale computations is plane-strain and thus is representative of fibres with a relatively large (actually infinite) length. The fibres and the epoxy matrix are meshed with 6-node triangular elements equipped with a 7-point Gauss quadrature. Debonding between fibre and matrix is simulated with the interface damage model summarised in Section 2, using 6-node interface elements equipped with a 3-point Newton-Cotes quadrature.

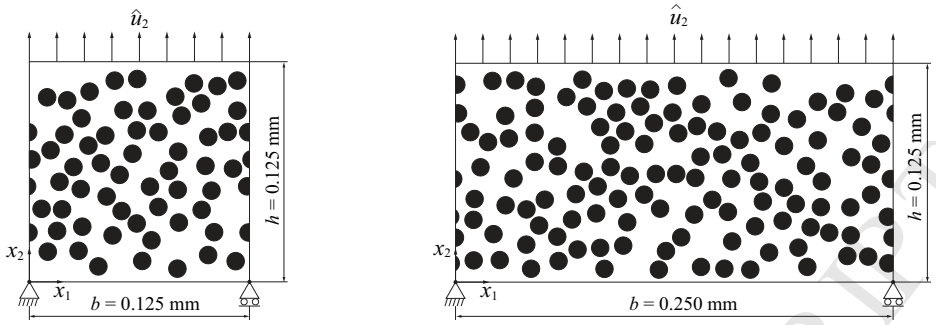

(a) Square-shaped specimen. (b) Rectangular-shaped specimen.

Figure 4: Geometry and boundary conditions of fibre-epoxy samples with a **fibre volume fraction of 0.3**. The diameter of the glass fibres is 10μm.

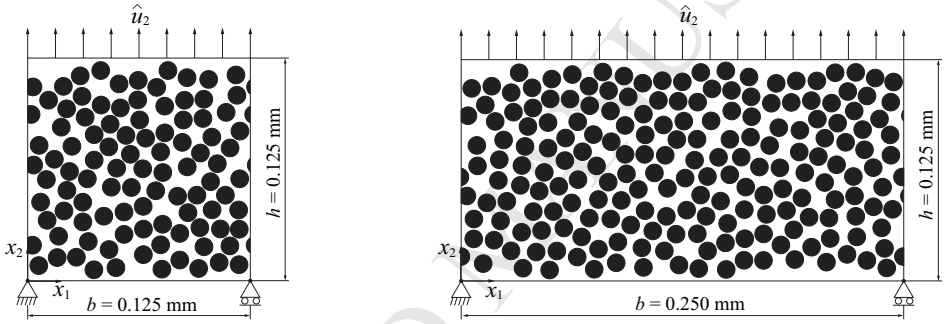

(a) Square-shaped specimen. (b) Rectangular-shaped specimen.

Figure 5: Geometry and boundary conditions of fibre-epoxy samples with a **fibre volume fraction of 0.5**. The diameter of the glass fibres is 10μm.

Fracture processes within the epoxy material are also simulated with the interface damage model, placing 6-node interface elements furnished with a 3-point Newton-Cotes quadrature in between triangular continuum elements constructing the epoxy matrix. This modelling approach for the simulation of fracture was originally proposed by Xu and Needleman [15], and warrants that the crack initiation and propagation processes in the sample are naturally determined by the geometry and boundary conditions applied, and by the parameter values used in the interface traction separation law. The influence of the finite element discretization on the fracture response can be minimised by choosing a sufficiently fine, randomly oriented mesh. Nonetheless, the mesh fineness is bounded by a maximum in or-

Sample shape	V_f	Continuum elements	Fibre-epoxy int. elems.	Epoxy int. elems.	Total
Square	0.3	5194	772	5001	10967
Square	0.5	9906	1679	6747	18332
Rectangular	0.3	10390	1549	10035	21974
Rectangular	0.5	19720	3360	13409	36489

Table 1: Number of elements used for samples of different size and volume fraction V_f, see Figures 4 and 5.

der to limit the artificial response contributions related to the use of an interface 'dummy' stiffness in the traction-separation law, see Eq.(1). In fact, the application of interface elements with an elastic dummy stiffness causes that the elastic response of the finite element model does not converge to that of an ideal continuum in the limit of an 'infinitely fine' mesh. The number of continuum elements and interface elements used in the finite element meshes of the samples in Figures 4 and 5 are listed in Table 1. Note from this table that the number of elements used for modelling the rectangular sample is about two times the number of elements used for the square sample. Mesh refinement studies reported in [18] indicate that for this mesh density the fracture response is computed with high accuracy.

The material parameters of the S2 glass fibre, the FM94 epoxy and the interfaces between fibres and epoxy and within the epoxy are listed in Table 2. The elastic material properties for the fibre and the epoxy matrix have been adopted from [26]. The value of the elastic stiffness K of the interfaces is taken relatively high, such that the interfacial deformations in the elastic regime are negligibly small. Values for the ultimate strengths and toughnesses of the epoxy material and of fibre-epoxy interface could not be found in the literature, and therefore are estimated from the failure response of delamination tests on double spliced GLARE specimens [27]. The toughness values listed in Table 2 indicate that the FM94 epoxy used in these experimental specimens is relatively brittle, both in tension and in shear. It is worth mentioning that the prepreg layer of a more recent generation of GLARE laminates is a factor 5 to 8 tougher, due to improvements in the manufacturing process and the use of an improved epoxy material with better mechanical properties, see [28]. For simplicity, for the epoxy and fibre-epoxy interfaces the strength and toughness values are taken the same. Here, the subscripts 'coh' and 'adh' used in the denotation of the parameters refer to the cohesive strength of the epoxy material and the adhesive strength of the fibre-epoxy inter-

Parameter(s)	*Value(s)*
Fibre	
Young's modulus	E = 86.9 [GPa]
Poisson's ratio	ν = 0.23
Epoxy	
Young's modulus	E = 3.9 [GPa]
Poisson's ratio	ν = 0.37
Fibre-epoxy interface & epoxy interface	
Elastic stiffness	K = 1×10^8 [N/mm^3]
Ultimate normal and shear strengths	$t_1^u = t_2^u = t_{adh}^u$ = 50 [MPa]
Mode I and mode II fracture toughnesses	$G_{I,c} = G_{II,c} = G_{c,adh}$ = 0.5 [N/mm]
Relaxation parameter	η = 0.002 [s]

Table 2: Material properties of the fibre-epoxy sample.

face, respectively. The value of the relaxation parameter η is taken relatively small in order to closely approach the limit case of rate-independent crack growth. Additional simulations not presented here have shown that the introduction of a small rate-dependency is necessary to avoid numerical convergence problems caused by crack bifurcations.

5.3. Influence of sample size and fibre volume fraction

The failure responses of the samples with the two different widths are mutually compared to assess the convergence of the numerical result upon an increasing microstructural sample volume, see also, for example, [9]. The mesoscopic traction-separation relation obtained after applying the homogenization approach presented in Section 4.3.2 to the numerical results is shown in Figure 6. It can be observed that for both volume fractions the traction-separation responses of the square-shaped and rectangular-shaped samples are similar, indicating that the square-shaped sample is sufficiently large for being considered as an RVE. Essentially, the traction-separation responses closely follow the mode I traction-separation law of the epoxy material. This is due to the fact that the failure process develops locally through the epoxy material in a mode I dominated fashion (i.e., the orientation of the failure crack is approximately perpendicular to the direction of the tensile loading). This can be observed from Figures 7 and 8 for the square-shaped and rectangular shaped specimens with a fibre volume fraction of

0.3, respectively, and from Figures 9 and 10 for the square-shaped and rectangular shaped specimens with a fibre volume fraction of 0.5, respectively. In all cases the crack clearly grows through the fibre-low (or epoxy-rich) area close to the top edge of the specimen. This position of the dominant failure crack is in agreement with experimental observations on delamination failure in fibre-metal laminates [13]. These experiments show that mesoscale delamination between the prepreg layer and the aluminium layer at the microscale occurs by cracking at the edge of the fibre-low area, which is close to the edge of the prepreg layer, see Figure 11. Since the fibres are hardly involved in this failure mechanism, a change in the fibre volume fraction from 0.3 to 0.5 changes the sample response only mildly. Because the present analysis shows that the square-shaped sample can be considered as a representative volume element, this sample will be used for the forthcoming computations in this communication.

5.4. Influence of imperfections on failure response

In order to study how the homogenized traction-separation response is influenced by imperfections at fibre-epoxy interfaces, four different configurations are considered, see Figure 12. The fibre volume fraction of the sample is 0.3 and the imperfections are represented by a local absence of the adhesive bonding strength

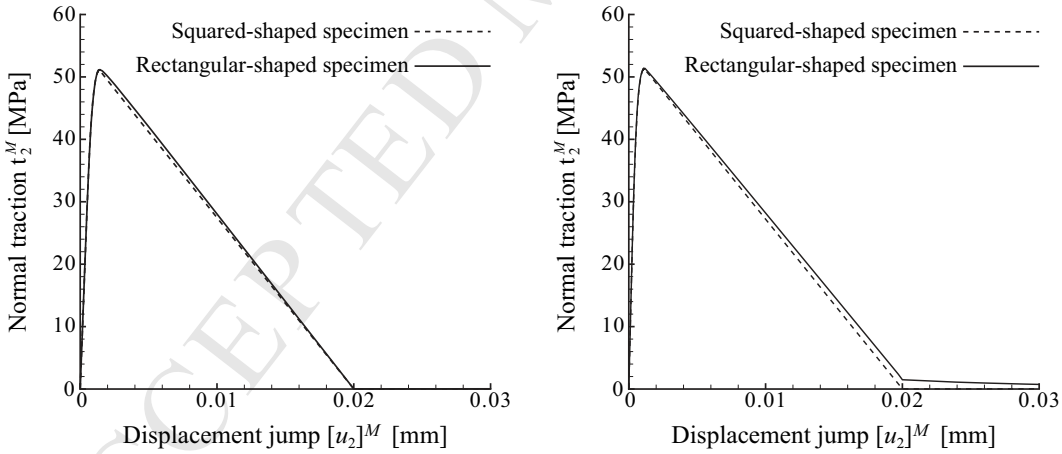

(a) Fibre volume fraction $V_f = 0.3$ (b) Fibre volume fraction $V_f = 0.5$

Figure 6: Mesoscopic traction-separation response for the square-shaped and rectangular-shaped samples shown in Figures 4 and 5. a) Fibre volume fraction V_f=0.3. b) Fibre volume fraction V_f = 0.5.

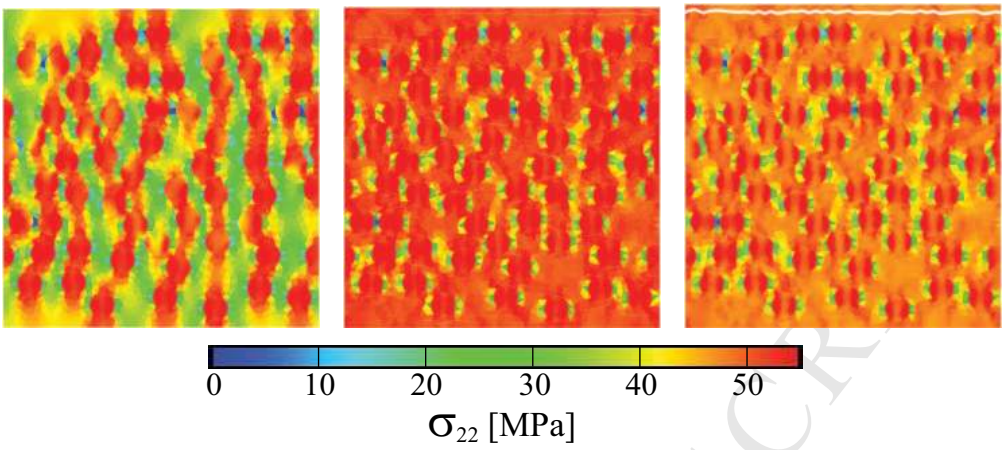

Figure 7: Axial normal stress σ_{22} depicted in deformed, cracked configurations, for the square-shaped sample in Figure 4(a) (which has a **fibre volume fraction of 0.3**). The deformed states are taken at relative displacements $[\![u_2]\!]^M = 0.000816, 0.00146$ and 0.00257 mm, respectively.

at specific fibre-epoxy interfaces. As illustrated in Figure 12, the four configurations considered are characterised by: (i) A single imperfection in the upper region of the sample (i.e., in the left-top quadrant), (ii) A single imperfection in the lower region of the sample (i.e., in the right-bottom quadrant), (iii) Two imperfections in the upper and lower regions of the sample (i.e., a combination of configurations (i) and (ii)), and (iv) Two imperfections in the upper and lower regions of the sample, where the upper imperfection coincides with that in configuration (i) and the lower imperfection is placed somewhat higher than that of configuration (ii).

The mesoscopic traction-separation response for the different configurations in Figure 12 is plotted in Figure 13. For comparison, the response of the specimen without imperfections, plotted in Figure 6(a), has also been included in this figure. The corresponding fracture patterns are depicted in Figures 14 to 17. For all configurations the imperfections clearly act as nucleation sites for crack development. In addition, their location typically is included in the geometry of the dominant failure crack that develops upon complete failure of the fibre-epoxy specimen. An exception in this respect, however, is the imperfection located in the upper half of configuration (iii), see Figure 16; this imperfection initially acts as a nucleation site for cracking but eventually is not included in the geometry of the dominant failure crack, due to a local unloading upon deformation. This is an important difference with configuration (iv), where *both* imperfections are

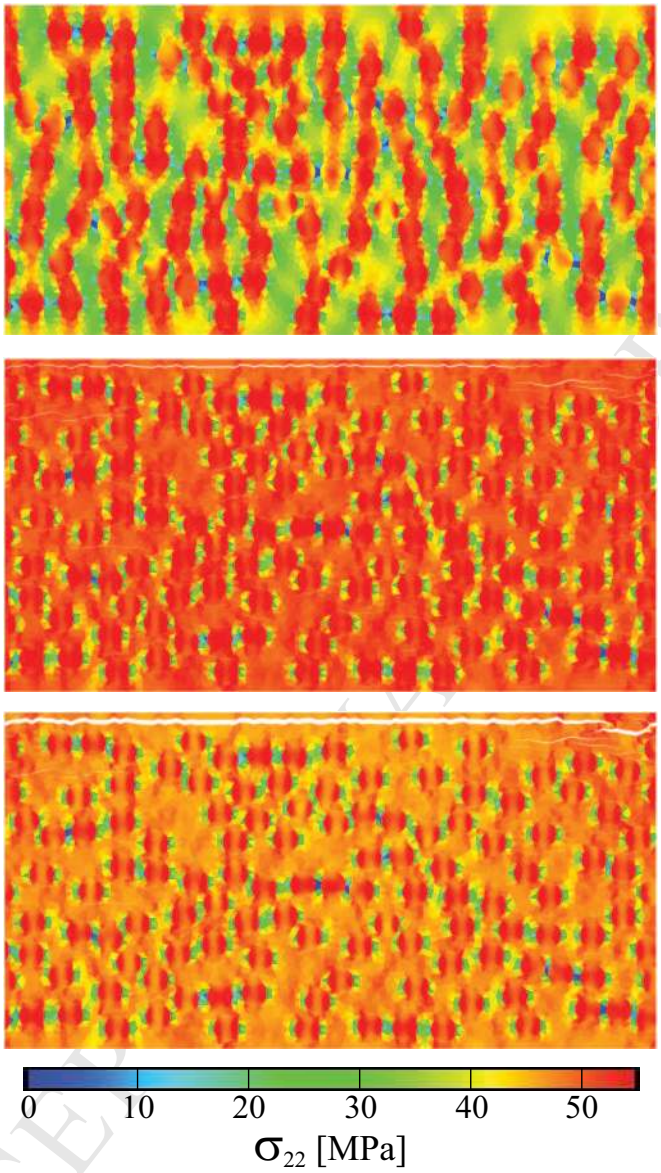

Figure 8: Axial normal stress σ_{22} depicted in deformed, cracked configurations, related to the rectangular-shaped sample in Figure 4(b) (which has a **fibre volume fraction of 0.3**). The deformed states are taken at relative displacements $[\![u_2]\!]^M = 0.000815, 0.00186$ and $0.00314\,\text{mm}$, respectively.

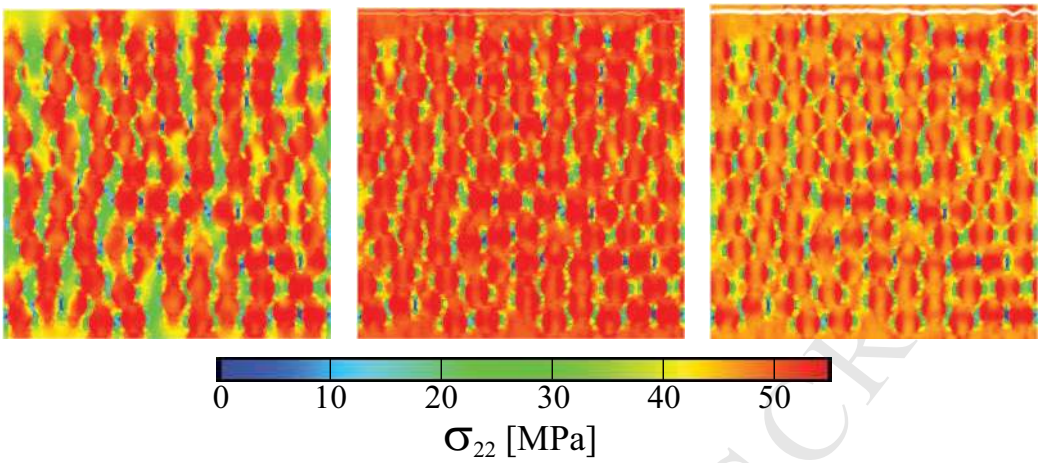

Figure 9: Axial normal stress σ_{22} depicted in deformed, cracked configurations, related to the square-shaped sample in Figure 5(a) (which has a **fibre volume fraction of 0.5**). The deformed states are taken at relative displacements $[\![u_2]\!]^M = 0.000669, 0.00136$ and 0.00265 mm, respectively.

included in the geometry of the dominant failure crack, see Figure 17. The net result of this behaviour is that the total crack length of configuration (iv) is substantially larger than that of configuration (iii), which thus requires more energy dissipation in order to fail the sample. Correspondingly, the effective fracture toughness of configuration (iv) is larger than that of configuration (iii), see Figure 13, and also is larger than that of the sample without imperfections. Hence, it may be concluded that the presence of imperfections in a fibre-epoxy sample may have a positive effect on the effective fracture toughness. From the comparison of the fracture patterns for configurations (iii) and (iv) it can be further concluded that the two imperfections *both* contribute to the geometry of the dominant failure crack (thereby enhancing the effective fracture toughness) *only* if the distance between the imperfections in the tensile direction (i.e., in the thickness direction of the layer) is not too large.

6. Concluding remarks

In this paper a numerical homogenization framework has been presented that links the microscale response of a fibre-epoxy sample to a mesoscale traction-separation curve that can be used for simulating the failure response of a (material point in a) cohesive interface. The formulation is based on Hill's averaging prin-

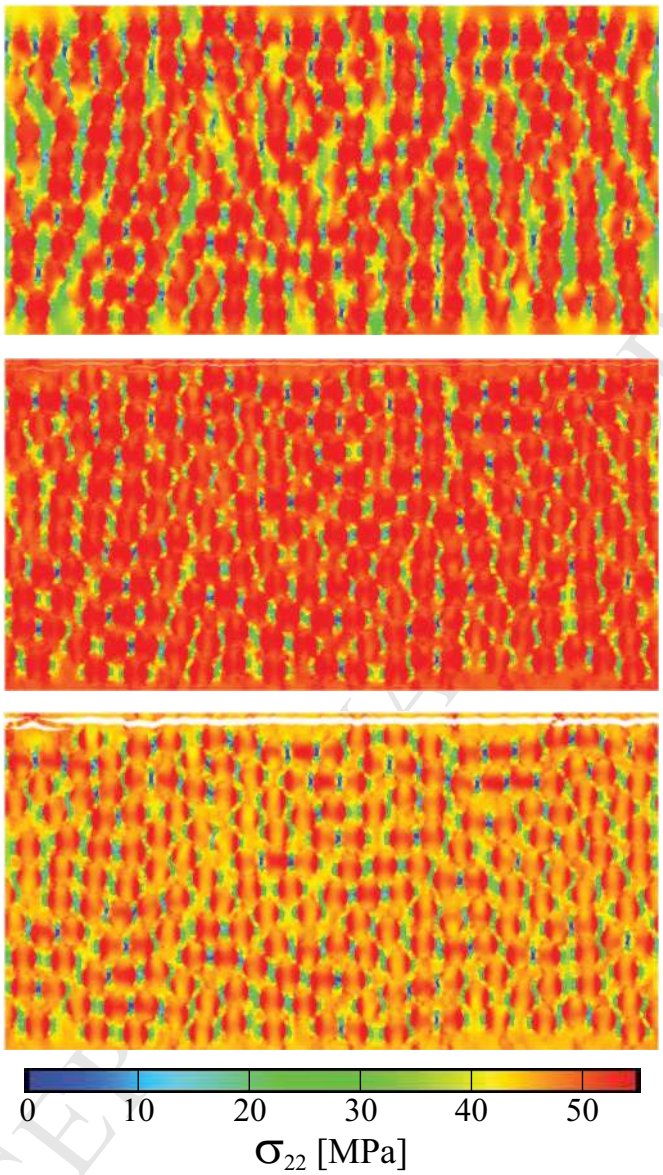

Figure 10: Axial normal stress σ_{22} depicted in deformed, cracked configurations, related to the rectangular-shaped sample in Figure 5(b) (which has a **fibre volume fraction of 0.5**). The deformed states are taken at relative displacements $[\![u_2]\!]^M = 0.000669, 0.00134$ and 0.00345 mm, respectively.

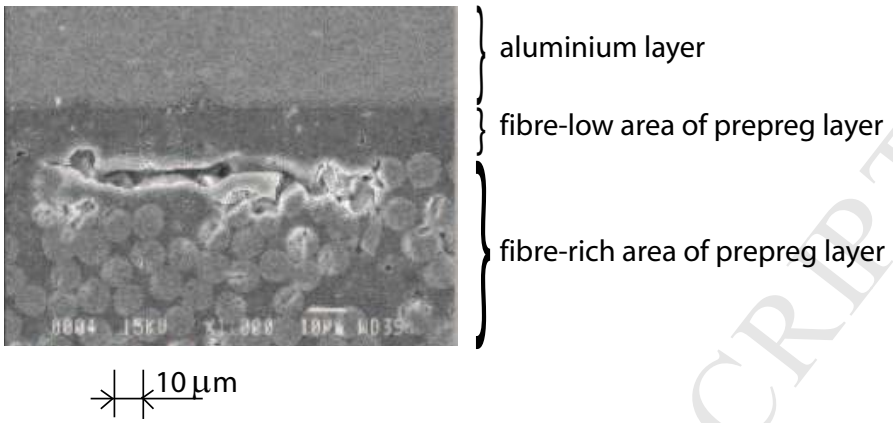

Figure 11: A delaminating crack in a fibre-metal laminate, taken from [13]. The crack propagates at the transition between the fibre-low and fibre-rich areas of the prepreg layer, which is close to the interface with the aluminium layer.

ciple, which states that the spatial average of the virtual work at the microscale is equal to the virtual work in a local material point of the mesoscale cohesive interface. Microscale numerical simulations are performed on a fibre-epoxy sample subjected to uniaxial tension. Two different sample sizes are analysed for two different values of the fibre volume fraction, $V_f = 0.3$ and 0.5. When the interface between fibres and epoxy is of a higher strength than the epoxy itself, the numerical response is characterised by a failure pattern that develops mainly through the epoxy matrix, as a result of which the failure response is not very sensitive to a change in the fibre volume fraction. The numerical results converge upon

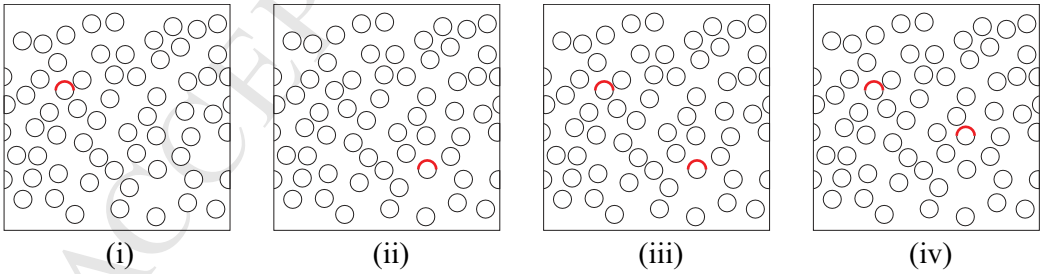

Figure 12: Four fibre-epoxy samples with different locations and/or number of imperfections. The fibre volume fraction of the sample is 0.3 and imperfections are indicated in red.

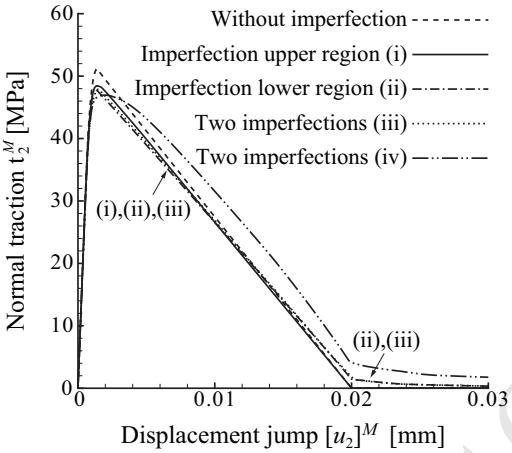

Figure 13: Mesoscopic traction-separation law corresponding to the square-shaped sample with a fibre volume fraction of 0.3 (shown in Figure 4(a)), plotted for a different number and position of imperfections, see Figure 12.

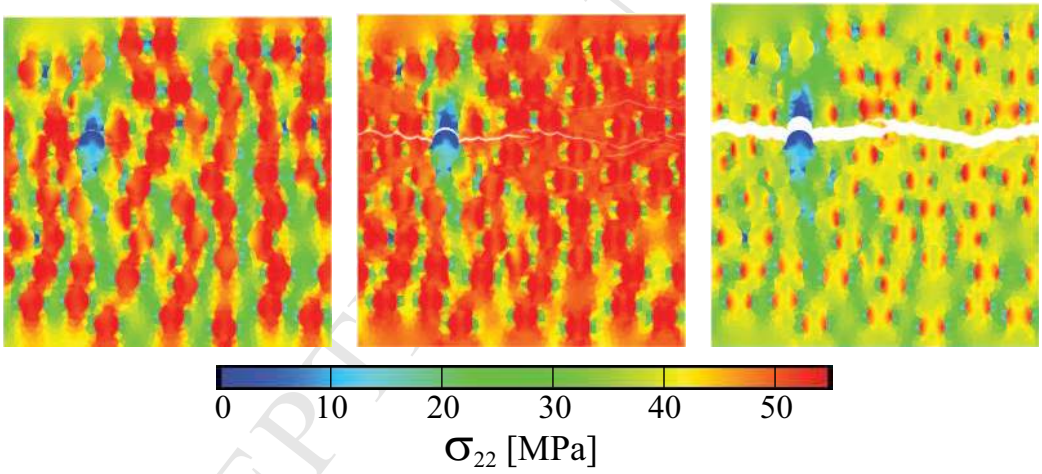

Figure 14: Axial normal stress σ_{22} depicted in deformed, cracked configurations, for **case (i)** in Figure 12. The deformed states are taken at $[\![u_2]\!]^M = 0.821, 1.940$ and $5.985\ \mu$m, respectively.

increasing the sample size, confirming that the sample size approaches a representative volume element (RVE). The influence on the effective sample response by the number and position of initial imperfections within the specimen is also

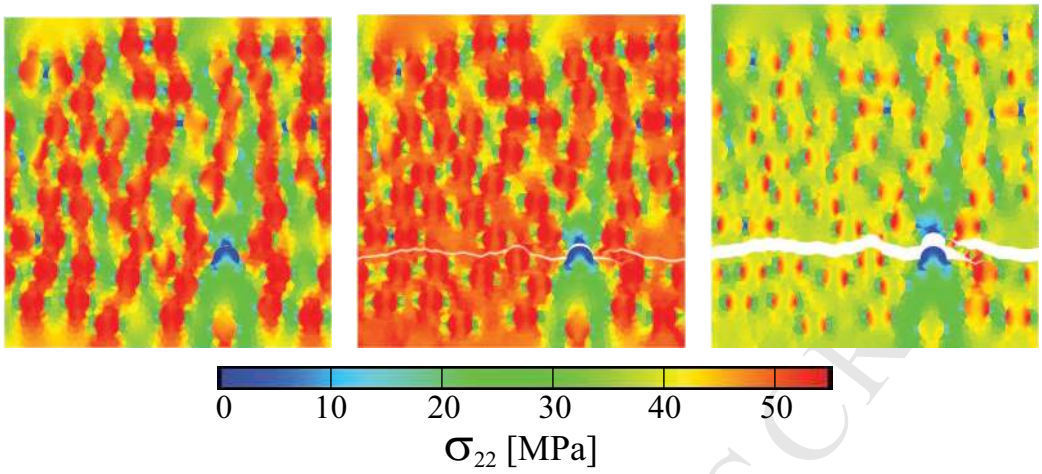

Figure 15: Axial normal stress σ_{22} depicted in deformed, cracked configurations, for **case (ii)** in Figure 12. The deformed states are taken at $[\![u_2]\!]^M = 0.821, 1.854$ and $5.863\,\mu$m, respectively.

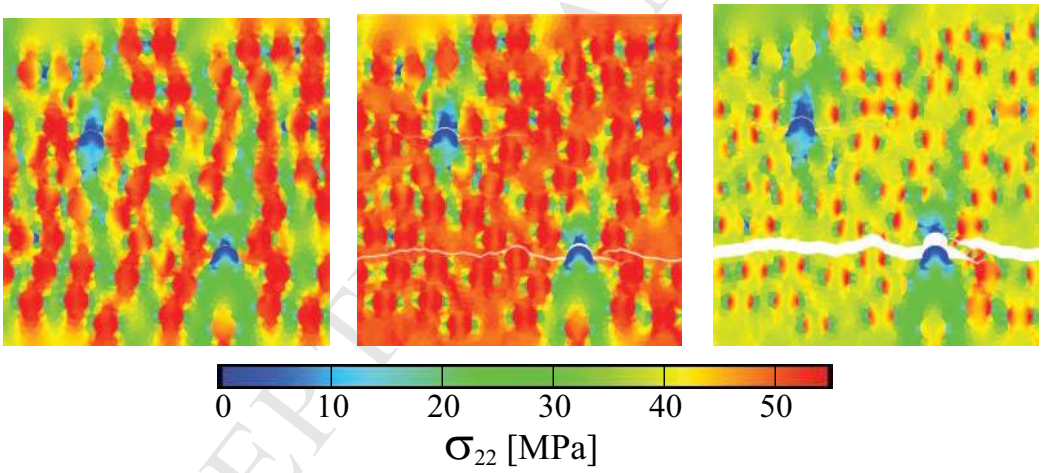

Figure 16: Axial normal stress σ_{22} depicted in deformed, cracked configurations, for **case (iii)** in Figure 12. The deformed states are taken at $[\![u_2]\!]^M = 0.821, 1.985$ and $5.894\,\mu$m, respectively.

studied. The imperfections generally trigger crack nucleation, and their location typically is included in the geometry of the dominant failure crack that develops upon deformation. As a result of this behaviour, imperfections can increase the

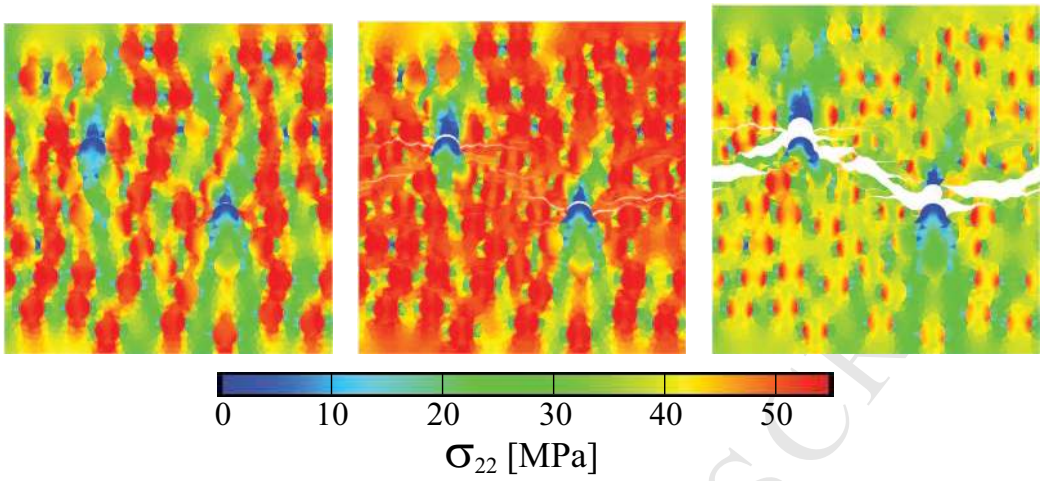

Figure 17: Axial normal stress σ_{22} depicted in deformed, cracked configurations, for the **case (iv)** in Figure 12. The deformed states are taken at $[\![u_2]\!]^M = 0.822, 1.856$ and 8.041 μm, respectively.

length of the dominant failure crack (as compared to the crack length for a sample without imperfections), and thus may enhance the effective fracture toughness of the sample.

The present numerical homogenization technique computes the complex failure response of fibre-epoxy samples in a robust and accurate manner. Although the examples studied are limited to fibre-epoxy samples subjected to uniaxial tension, it is emphasised that the averaging relations proposed in Section 4.2, in principle, can be applied to *arbitrary* mixed-mode (i.e., tensile and shear) loading conditions.

The simulations for fibre-epoxy samples loaded under uniaxial tension have shown that the differences between the effective failure response of the fibre-epoxy layer and the microscopic failure behaviour of the epoxy matrix are small, see Figure 6. This is partly due to the fact that the cracking processes are described with a discrete damage model, which makes it possible to capture a local, mode I-driven failure behaviour in an accurate fashion. A more diffusive, continuum damage model, such as that used by Geubelle and co-workers in their homogenisation framework [10, 11], by definition will lead to a larger difference between the local failure behaviour and the effective failure response of a fibre-epoxy layer. It is also expected that under mixed-mode loading conditions this difference will be larger than under the mode I loading conditions studied in this manuscript,

since under increasing mode-mixity the fracture patterns in fibre-epoxy systems typically become more distributive (or less localised), see [11]. In addition, as observed in recent micromechanical computations [29], this difference may further become larger when the strength of the fibre-epoxy interface is lower than the strength of the epoxy. This is, because under such conditions the cracking path is forced to run along the perimeter of fibres and consequently increases in length, thereby enlarging the effective fracture toughness of the fibre-epoxy system (similar to what has been demonstrated in this paper for samples with imperfections at fibre-epoxy interfaces). These issues are interesting topics for future studies.

Acknowledgements

This work is part of the research project DLR.5790 - DFG 509 "Multiscale Methods in Computational Mechanics". The authors gratefully acknowledge the financial support of this research project by the *Stichting Technische Wetenschappen* (STW), the Netherlands, and the *Deutsche Forschungsgemeinschaft* (DFG), Germany.

References

[1] P.M. Suquet. *Local and global aspects in the mathematical theory of plasticity*. In Sawczuk, A. and Bianchi, G., eds, Plasticity today: modelling, methods and applications, pages 279–310. Elsevier Applied Science Publishers, London, 1985.

[2] J.M. Guedes and N. Kikuchi. Preprocessing and postprocessing for materials based on the homogenization method with adaptive finite-element methods. *Computer Methods in Applied Mechanics and Engineering*, 83:143–198, 1990.

[3] S. Ghosh, K. Lee, and S. Moorthy. Multiple scale analysis of heterogeneous elastic structures using homogenization theory and Voronoi cell finite element method. *International Journal of Solids and Structures*, 32:27–62, 1995.

[4] S. Ghosh, K. Lee, and S. Moorthy. Two scale analysis of heterogeneous elastic-plastic materials with asymptotic homogenization and Voronoi cell finite element model. *Computer Methods in Applied Mechanics and Engineering*, 132:63–116, 1996.

[5] C. Miehe, J. Schroder, and J. Schotte. Computational homogenization analysis in finite plasticity. Simulation of texture development in polycrystalline materials. *Computer Methods in Applied Mechanics and Engineering*, 171:387–418, 1999.

[6] V. Kouznetsova, W.A.M. Brekelmans, and F.P.T. Baaijens. An approach to micro-macro modeling of heterogeneous materials. *Computational Mechanics*, 27:37–48, 2001.

[7] V. Kouznetsova, M.G.D. Geers, and W.A.M. Brekelmans. Multi-scale constitutive modelling of heterogeneous materials with a gradient-enhanced computational homogenization scheme. *International Journal for Numerical Methods in Engineering*, 54:1235–1260, 2002.

[8] C. Miehe and A. Koch. Computational micro-to-macro transitions of discretized microstructures undergoing small strains. *Archive Of Applied Mechanics*, 72:300–317, 2002.

[9] C. Pelissou, J. Baccou, Y. Monerie, and F. Perales. Determination of the size of the representative volume element for random quasi-brittle composites. *International Journal of Solids and Structures*, 46:2842–2855, 2009.

[10] K. Matouš, M.G. Kulkarni, and P.H. Geubelle. Multiscale cohesive failure modeling of heterogeneous adhesives. *Journal of the Mechanics and Physics of Solids*, 56:1511–1533, 2008.

[11] M.G. Kulkarni, P.H. Geubelle, and K. Matouš. Multi-scale modelling of heterogeneous adhesives: Effect of particle decohesion. *Mechanics of Materials*, 41:573–583, 2009.

[12] E.K. Gamstedt and B.A. Sjogren. Micromechanisms in tension-compression fatigue of composite laminates containing transverse plies. *Composites Science and Technology*, 59:167–178, 1999.

[13] A. Vlot and J. W. Gunnink. *Fibre metal laminates - An introduction*. Kluwer Academic Publishers, Dordrecht, 2001.

[14] T. Hobbiebrunken, M. Hojo, T. Adachi, C. de Jong, and B. Fiedler. Evaluation of interfacial strength in CF/epoxies using FEM and in-situ experiments. *Composites Part A*, 38:2248–2256, 2006.

[15] X.P. Xu and A. Needleman. Numerical simulations of fast crack growth in brittle solids. *Journal of the Mechanics and Physics of Solids*, 42:1397–1407, 1994.

[16] M.G.A. Tijssens, E. van der Giessen, and L.J. Sluys. Simulation of mode I crack growth in polymers by crazing. *International Journal of Solids and Structures*, 37:7307–7327, 2000.

[17] M.G.A. Tijssens, L.J. Sluys, and E. van der Giessen. Simulation of fracture of cementitious composites with explicit modeling of microstructural features. *Engineering Fracture Mechanics*, 68:1245–1263, 2001.

[18] M.V. Cid Alfaro. *Multiscale Analyses of Fibre Metal Laminates*. PhD thesis, Delft University of Technology, Delft, 2008.

[19] M.V. Cid Alfaro, A.S.J. Suiker, R. de Borst, and J.J.C. Remmers. Analysis of fracture and delamination in laminates using 3D numerical modelling. *Engineering Fracture Mechanics*, 76:761–780, 2009.

[20] A.S.J. Suiker and N.A. Fleck. Crack tunneling and plane-strain delamination in layered solids. *International Journal of Fracture*, 125:1–32, 2004.

[21] A.S.J. Suiker and N.A. Fleck. Modelling of fatigue crack tunneling and delamination in layered composites. *Composites Part A: Applied Science and Manufacturing*, 37:1722–1733, 2006.

[22] A. Turon, P.P. Camanho, J. Costa, and C.G. Davila. A damage model for the simulation of delamination in advanced composites under variable-mode loading. *Mechanics of Materials*, 38:1072–1089, 2006.

[23] J.W. Hutchinson and Z. Suo. Mixed mode cracking in layered materials. *Advances in Applied Mechanics*, 29:63–191, 1992.

[24] H.M. Jensen. Mixed mode interface fracture criteria. *Acta Metallurgica et Materialia*, 38:2637–2644, 1990.

[25] R. Hill. The essential structure of constitutive laws for metal composites and polycrystals. *Journal Of The Mechanics And Physics Of Solids*, 15:79–95, 1967.

[26] M. Hagenbeek. *Characterization of Fibre Metal Laminates under Thermo-mechanical loadings*. PhD thesis, Delft University of Technology, Delft, 2005.

[27] F. Hashagen and R. de Borst. Numerical assessment of delamination in fibre metal laminates. *Computer Methods in Applied Mechanics and Engineering*, 185:141–159, 2000.

[28] J. van den Brande and J. Sinke. FIMELAS - numerical modelling of fibre-metal laminates: microscopic damage models. Technical Report B2V-04-02, Delft University of Technology, Netherlands, 2004.

[29] M.V. Cid Alfaro, A.S.J. Suiker, and R. de Borst. Off-axis behaviour of fibre-epoxy systems. Submitted for publication, 2009.